The Astrophysical Journal Letters, 1010:L9 (14pp), 2026 October 10 https://doi.org/10.3847/2041-8213/aeaa29
© 2026. The Author(s). Published by the American Astronomical Society.
OPEN ACCESS

The PSR J0435+3233 Triple System

Z. L. Yang[1], J. L. Han[1,2,3], Yi Yan[1], Bin Liu[4], Y. L. Guo[5], M.K. Yang[5], Bo Wang[5], Wei-Min Gu[6], J. Li[5], L. H. Li[5], J. Xu[1,3], and Jian-Ning Fu[7,8]
[1] National Astronomical Observatories, Chinese Academy of Sciences, Jia-20 Datun Road, Chaoyang District, Beijing 100012, People's Republic of China; hjl@nao.cas.cn
[2] School of Astronomy and Space Science, University of Chinese Academy of Sciences, Beijing 100049, People's Republic of China
[3] State Key Laboratory of Radio Astronomy and Technology, Beijing 100101, People's Republic of China
[4] Institute for Astronomy, School of Physics, Zhejiang University, 310058, Hangzhou, People's Republic of China
[5] International Center of Supernovae (ICESUN), Yunnan Key Laboratory of Supernova Research, Yunnan Observatories, Chinese Academy of Sciences (CAS), Kunming 650216, People's Republic of China
[6] Department of Astronomy, Xiamen University, Xiamen, Fujian 361005, People's Republic of China
[7] Institute for Frontiers in Astronomy and Astrophysics, Beijing Normal University, Beijing 102206, People's Republic of China
[8] School of Physics and Astronomy, Beijing Normal University, Beijing 100875, People's Republic of China
Received 2026 July 31; revised 2026 September 17; accepted 2026 September 19; published 2026 October 8

Abstract

The detailed evolution of triple star systems is complicated and poorly known. Using archived optical/infrared and gamma-ray data, we identified the pulsar PSR J0435+3233 as a gamma-ray pulsar in a hierarchical triple system, with a helium white dwarf (WD) as a close inner binary companion and a Sun-like star as the distant tertiary. PSR J0435+3233 and the WD companion are in a circular orbit with a period of $P_{\rm orb1} = 8.0$ days and an eccentricity of $e = 0.00016$. The tertiary is a G-type subgiant with a mass of $0.98(12)\,M_{\odot}$ at a distance of 2.1(4) kpc from the Earth. By simultaneously fitting the observed spin-period variations of the gamma-ray emission (over 16.7 yr) and radio emission (over 4.9 yr) from PSR J0435+3233, the changes in the inner orbital parameters, the Shapiro delay, Gaia astrometry, and the outer companion mass, we determined the outer elliptical orbit for the tertiary, with a period $P_{\rm orb2} = 73.5$ yr and an eccentricity $e_2 = 0.598$. The outer orbit is either nearly perpendicular to the inner orbit with a mutual inclination of $\sim 85^{\circ}$, or moderately inclined by $\sim 54^{\circ}$. For the former geometry, the pulsar, the WD, and the tertiary star have masses of $1.16(5)\,M_{\odot}$, $0.273(8)\,M_{\odot}$, and $0.91(5)\,M_{\odot}$, respectively; for the latter geometry, the corresponding masses are $1.34(15)\,M_{\odot}$, $0.305(23)\,M_{\odot}$, and $1.13(7)\,M_{\odot}$. This is a unique triple system for detailed multiband observations and for studying the evolutionary path and dynamic processes of a primordial triple star system. It will ultimately evolve into a system consisting of a neutron star and two WDs.

Unified Astronomy Thesaurus concepts: Neutron stars (1108); Binary pulsars (153); Trinary stars (1714)

1. Introduction

Optical surveys suggested that a substantial fraction of intermediate- and high-mass stars reside in hierarchical triple systems (M. Moe & R. Di Stefano 2017), with the triple fraction reaching approximately 20%–30% and even higher for the most massive stars. A hierarchical triple system can remain dynamically stable if the tertiary star orbits the inner binary on a sufficiently wide orbit (R. A. Mardling & S. J. Aarseth 2001). Naturally, the massive stars in the triple system evolve and can produce black holes or neutron stars (NSs), while stars with intermediate or small masses produce white dwarfs (WDs). Therefore, some triple systems could have zero, one, two, or even three compact components, depending on the system's evolutionary stage.

Millisecond pulsars in gravitationally bound three-body systems are extremely rare. They are valuable samples for stellar evolution studies and also probes for tests of gravitational theories. PSR B1620–26 (S. E. Thorsett et al. 1999) is in a triple system, with the outer companion being an ultralight object. PSR J0337+1715 has two WD companions in two near-circular orbits (S. M. Ransom et al. 2014). The relatively high masses of the two WD companions of PSR J0337+1715 make gravitational three-body effects significant, and unique gravity tests have been performed based on the timing of this pulsar (L. Shao 2016; L. Iorio 2024). The evolution of triple systems with pulsars has also drawn much attention. Many formation scenarios for PSR J0337+1715 have also been proposed (T. M. Tauris & E. P. J. van den Heuvel 2014; E. Sabach & N. Soker 2015; G. Voisin et al. 2020). Further evolution of the PSR J0337+1715 triple system can produce isolated millisecond pulsars or millisecond pulsars in eccentric orbits (S. Portegies Zwart et al. 2011).

The millisecond radio pulsar PSR J0435+3233, with a period of $P = 3.20$ ms, was discovered by Q. Wu et al. (2026) using the Five-hundred-meter Aperture Spherical radio Telescope (FAST; R. Nan 2006) during the Commensal Radio Astronomy FAST Survey (CRAFTS; D. Li et al. 2018). After long-term efforts on pulsar timing, Q. Wu et al. (2026) found that it has an extremely large period derivative compared to other known millisecond pulsars, and has been identified as a binary pulsar moving in an 8 day orbit, with a likely helium WD (He WD) companion of mass $\sim 0.3\,M_{\odot}$. They also found that the orbital parameters of PSR J0435+3233 vary rapidly.

We detected the gamma-ray emission from PSR J0435+3233 using the Fermi data (S. Abdollahi et al. 2022) and identified a Sun-like G-type subgiant as its second companion,

Original content from this work may be used under the terms of the Creative Commons Attribution 4.0 licence. Any further distribution of this work must maintain attribution to the author(s) and the title of the work, journal citation and DOI.

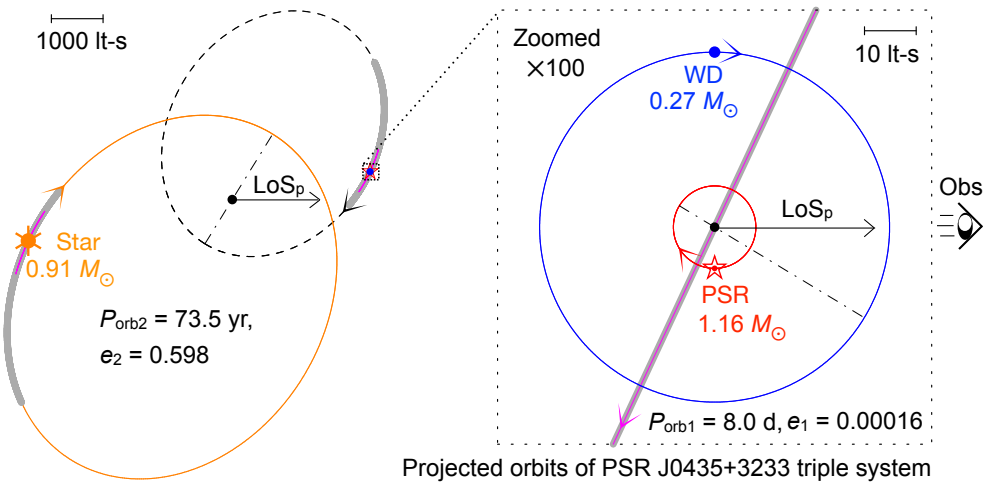


Figure 1. Projected orbits of PSR J0435+3233 and its companions along the line of sight (based on the final timing solution A). The two black dots indicate the barycenters of the inner and outer orbits. The pulsar and the inner WD companion revolve clockwise around the inner barycenter with a period of 8 days, while the inner binary as a whole revolves clockwise around the triple-system barycenter with a period of about 73.5 yr. The line-of-sight ($\mathrm{LoS_p}$) is indicated by black arrows starting from the system's barycenters. The orbits shown here are the apparent orbits projected along the line of sight (the true orbital separation multiplied by $\sin i$). The red star marks the pulsar position at the epoch T_{asc1} = MJD 59997.48 (as listed in Table 1), the blue dot marks the position of the inner WD companion, and the orange dot marks the position of the outer star companion. The two gray dotted–dashed lines connect the orbits' periastrons. The magenta line indicates the motion of the inner binary barycenter during the FAST data span, while the thick gray line indicates its motion during the long Fermi data span.

confirming that PSR J0435+3233 is in a triple system comprising a gamma-ray millisecond pulsar, a WD, and a Sun-like star (see Figure 1). By accounting for the observed spin-period and orbital-parameter variations of PSR J0435+3233 induced by the gravitational perturbation from this tertiary, we determined the outer elliptical orbit, masses, and geometries. While preparing the submission of this Letter, we noticed that P. Freire et al. (2026) worked independently on this object and obtained similar results, confirming each other well despite very different details. In the following, we present our data analyses and results, from the FAST radio data to the optical identification and long-term gamma-ray data, and demonstrate how these data together constrain the properties of the PSR J0435+3233 triple system.

2. Identification of the PSR J0435+3233 Triple System

We identified the PSR J0435+3233 triple system from the FAST radio data, archived optical/infrared images, and Fermi data.

2.1. Reprocessing the FAST Archive Data and Timing PSR J0435+3233

PSR J0435+3233 has been observed by FAST for 192 sessions in the last 5 yr (Q. Wu et al. 2026) using the 19-beam *L*-band receiver (P. Jiang et al. 2020). All FAST observations of PSR J0435+3233 cover a frequency range of 1.0 to 1.5 GHz, and the data of all sessions were recorded in four polarization channels: *XX*, *YY*, Re[*XY*], and Im[*XY*]. At the beginning of most observations, the calibration noise signals with an amplitude of 12.5 K and a period of 0.100663 s were injected into the receiver feeds for 40 s, thereby enabling polarization calibration.

We reprocessed the released FAST archive data of 192 sessions in the MJD range from 59101 to 60877 for timing PSR J0435+3233. We folded the raw data using DSPSR (W. van Straten & M. Bailes 2011), producing pulse polarization profiles with 128 phase bins across the pulse longitude. Polarization calibration was then applied via the `pac` routine within the PSRCHIVE package (A. W. Hotan et al. 2004). For each session, we obtained the polarization profiles for four frequency subbands. The pulsar shows strong scintillation. We built the standard profile using the `paas` command (A. W. Hotan et al. 2004) from the observation with the highest flux density. Then we extracted pulse times of arrival (TOAs) with the `pat` command (A. W. Hotan et al. 2004). We refined the DM value by comparing TOAs in four subbands, then extracted TOAs from integrated profiles of 192 sessions. Based on the derived TOAs, we performed pulsar timing analysis using the TEMPO2 software package (G. B. Hobbs et al. 2006). We shifted the spin-frequency reference epoch to MJD 59997.5, close to the ascending-node passage time T_{asc} (adopted as the orbital-frequency reference epoch). The TOA uncertainties have been multiplied by a factor EFAC to set the reduced χ^2 value to 1. Table 1 lists the final timing solutions and derived parameters, and Figure 2 plots the corresponding timing residuals. Our timing results are consistent with those of Q. Wu et al. (2026), but show notable improvements in residuals and parameter accuracy.

The pulsar's close companion in the inner orbit is a WD. With the total mass of the inner binary, $M_{\mathrm{in}} = M_{\mathrm{PSR}} + M_{\mathrm{WD}}$, the mass function of the two compact objects in the inner orbit is

$$f(M_{\mathrm{in}}, M_{\mathrm{WD}}, i_1) = \frac{(M_{\mathrm{WD}} \sin i_1)^3}{M_{\mathrm{in}}^2} = \frac{4\pi^2}{G}\frac{x_1^3}{P_{\mathrm{orb1}}^2} = 0.0085233093(2)\, M_\odot, \quad (1)$$

where G is the gravitational constant.

In the ELL1H binary model (P. C. C. Freire & N. Wex 2010), the Shapiro-delay term is also expressed by a number of harmonics of the orbital period. In the triple system, however, we cannot measure the first two harmonics because they are coupled to the orbital parameters, while the outer companion's perturbation can introduce a systematic offset in the third harmonic h_3 (see below). Only the fourth harmonic h_4 is the smallest harmonic and free of perturbed bias, so it can be used for mass constraints. Based on the ELL1H binary model

Table 1
FAST Timing Model Parameters and Derived Quantities for PSR J0435+3233

Parameter	Value
General information	
MJD range	59,101– 60,877
Number of TOAs	192
EFAC value	1.03
Solar System ephemeris	DE440
Reference epoch (MJD)	59997.5
Binary model used	ELL1H
Model parameters	
R.A., α (J2000)	$04^{h}35^{m}33^{s}.760877(3)$
decl., δ (J2000)	$+32°33'07''.93339(18)$
Proper motion in R.A. (mas yr^{-1})	1.31(4)
Proper motion in decl. (mas yr^{-1})	−3.2(2)
Spin frequency, ν (Hz)	312.710325717587(2)
1st spin-frequency derivative, $\dot{\nu}$ (Hz s^{-1})	$-4.7677041(2)\times10^{-12}$
2nd spin-frequency derivative, $\ddot{\nu}$ (Hz s^{-1})	$-1.468823(2)\times10^{-20}$
3rd spin-frequency derivative, $\dddot{\nu}$ (Hz s^{-1})	$-7.31287(10)\times10^{-29}$
4th spin-frequency derivative, $\nu^{(4)}$ (Hz s^{-1})	$-4.5601(19)\times10^{-37}$
5th spin-frequency derivative, $\nu^{(5)}$ (Hz s^{-1})	$-2.892(4)\times10^{-48}$
6th spin-frequency derivative, $\nu^{(6)}$ (Hz s^{-1})	$-9.0(9)\times10^{-54}$
Dispersion measure, DM (pc cm^{-3})	37.32427(7)
Orbital frequency, $f_{\rm orb1}$ (Hz)	$1.44709060570(7)\times10^{-6}$
1st derivative of $f_{\rm orb1}$, $\dot{f}_{\rm orb1}$ (s^{-2})	$-2.2251(5)\times10^{-20}$
2nd derivative of $f_{\rm orb1}$, $\ddot{f}_{\rm orb}$ (s^{-3})	$-7.054(12)\times10^{-29}$
3rd derivative of $f_{\rm orb1}$, $\dddot{f}_{\rm orb1}$ (s^{-4})	$-3.79(13)\times10^{-37}$
Projected semimajor axis, x_1 (lt-s)	7.97814982(10)
1st derivative of x_1, $\dot{x}_1$ (lt-s s^{-1})	$6.043(17)\times10^{-13}$
2nd derivative of x_1, $\ddot{x}_1$ (lt-s s^{-2})	$1.87(8)\times10^{-22}$
Time of ascending-node passage, $T_{\rm asc1}$ (MJD)	59997.477140343(15)
First Laplace parameter, $\epsilon_1 = e_1 \sin\omega_1$	0.000139437(15)
Second Laplace parameter, $\epsilon_2 = e_1 \cos\omega_1$	−0.000084127(14)
3rd orthometric amplitude, h_3 (μs)	0.44(4)
4th orthometric amplitude, h_4 (μs)	0.34(6)
Derived parameters	
Spin period, P (s)	0.00319784771323193(3)
Orbital period, $P_{\rm orb1}$ (day)	7.9981682063(4)
Orbital eccentricity, e_1	0.000162850(15)
Longitude of periastron, ω_1 (deg)	121.104(5)
Mass function ($M_\odot$)	0.0085233088(3)

Note. These FAST timing solutions are derived with TEMPO2 (G. B. Hobbs et al. 2006) using the ELL1H binary model (C. Lange et al. 2001; P. C. C. Freire & N. Wex 2010) under the barycentric coordinate time (TCB) system. Uncertainties quoted in parentheses correspond to the 1σ errors for the last digit at the 68.3% confidence level.

(P. C. C. Freire & N. Wex 2010) with some modifications to include the high-order orbital-parameter derivatives, the Shapiro delay has been detected for the inner orbit in our timing analysis, yielding $h_3 = 0.44(4)\,\mu$s and $h_4 = 0.34(6)$. In general relativity (GR),

$$h_3 = \frac{GM_{\rm WD}}{c^3}\varsigma^3,$$
$$h_4 = \frac{GM_{\rm WD}}{c^3}\varsigma^4,$$
$$\varsigma = \left(\frac{\sin i_1}{1 + |\cos i_1|}\right)^{1/2}, \quad (2)$$

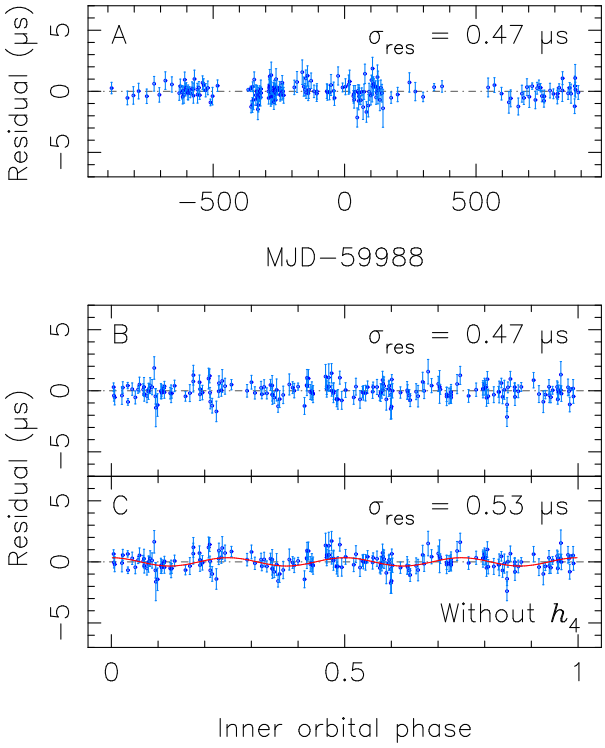


Figure 2. FAST timing residuals of PSR J0435+3233 based on the ELL1H model (see Table 1). Panel (A) shows the timing residuals across the observation dates (in MJD). Panels (B) and (C) show the residuals as a function of inner orbital phase (measured from the ascending-node passage) with and without considering the Shapiro-delay parameter h_4 in the timing model. The corresponding fourth harmonic terms are also indicated by the red line. The expected peak phase of the Shapiro-delay term is 0.25 when all harmonics are included.

where c is the speed of light. Hereafter, we take $c = 1$ and omit it in the following formula. The orbital inclination i_1 remains ambiguous because the standard Shapiro delay cannot distinguish between i_1 and $180° - i_1$. From these values, we obtained $M_{\rm WD} = \varsigma^{-4} \times 0.069(12)\,M_\odot$. Combining h_4 and the mass function, and assuming a typical pulsar mass of $M_{\rm PSR} = 1.4\,M_\odot$, we find an inclination angle for the orbital plane of $i_1 \sim 69°$ (or 111°) and a companion mass of $M_{\rm WD} \sim 0.31\,M_\odot$. Based on previous measurements (J. Alsing et al. 2018; B. Müller et al. 2025), NS masses are most likely to lie between 1.1 and $2.2\,M_\odot$. For the minimum pulsar mass of $M_{\rm PSR} = 1.1\,M_\odot$, the inclination angle should be $i_1 = 74°$ (or 106°), and the companion mass be $M_{\rm WD} = 0.26\,M_\odot$; for the maximum pulsar mass of $M_{\rm PSR} = 2.2\,M_\odot$, the inclination angle should be $i_1 = 66°$ (or 114°), and the companion mass is $M_{\rm WD} = 0.43\,M_\odot$. Therefore, the total mass of the inner binary should be between 1.4 and $2.6\,M_\odot$, and the inclination angle of the inner orbit should be $i_1 \sim 70°$ or 110°.

Millisecond pulsars with He WD companions that descend from low-mass X-ray binaries follow a $P_{\rm orb}$–$M_{\rm WD}$ relation (T. M. Tauris & G. J. Savonije 1999)

$$\frac{M_{\rm WD}}{M_\odot} = \left(\frac{P_{\rm orb}}{1.1 \times 10^5\ {\rm days}}\right)^{1/4.75} + 0.115. \quad (3)$$

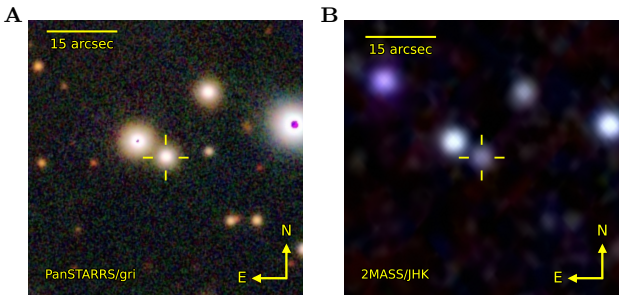


Figure 3. Optical and infrared counterpart of the outer companion of PSR J0435+3233. In the false-color image of Pan-STARRS (K. C. Chambers et al. 2016) and 2MASS (M. F. Skrutskie et al. 2006), a source is found at the location of PSR J0435+3233, which is the counterpart of its outer companion.

For the corresponding orbital period in Table 1, the derived He WD mass is 0.25 $M_{\odot}$, not much different from the abovederived mass.

Furthermore, we successfully detected the second derivative of the projected semimajor axis, $\ddot{x}$. After shifting the reference epoch of the orbital frequency and spin frequency to MJD 59997.5 (see Table 1), we found that the values of $\dot{\nu}/\nu = -1.5246 \times 10^{-14}\ \mathrm{s}^{-1}$ and $\dot{f}_{\mathrm{orb1}}/f_{\mathrm{orb1}} = -1.5382(3) \times 10^{-14}\ \mathrm{s}^{-1}$ are consistent up to 99%, indicating that the variations are caused by the tertiary in this system.

2.2. Identifying the Optical/infrared Counterpart as the Tertiary

At the almost exact position of PSR J0435+3233 (see Table 1), we found an optical and infrared counterpart (see Figure 3), Gaia DR3 1718333951761382 40, from the archived images or catalogs of the infrared and optical bands by the Pan-STARRS (K. C. Chambers et al. 2016), Gaia (Gaia Collaboration et al. 2016), TESS (G. R. Ricker et al. 2015), the Two Micron All Sky Survey (2MASS; M. F. Skrutskie et al. 2006), and Wide-field Infrared Survey Explorer (WISE; E. L. Wright et al. 2010). According to the Gaia DR3 (Gaia Collaboration et al. 2023) astrometry, at the reference epoch J2016.0 (MJD 57388.5), the star is located at R.A. $04^{\mathrm{h}}35^{\mathrm{m}}33^{\mathrm{s}}.761275(4)$ and decl. $+32^{\circ}33'07''.95514(4)$, with a proper motion of 0.694(84) mas yr^{-1} in R.A. and $-3.530(63)$ mas yr^{-1} in decl., consistent with the proper motion of the pulsar determined from the FAST timing observations (for the given the uncertainties).

Using measurements from these optical/infrared surveys, we can further determine the star's properties. The parallax of the star measured in Gaia DR3 (Gaia Collaboration et al. 2023) is 0.466(78) mas, corresponding to a distance of $D = 2.1(4)$ kpc. At this distance, the star has a bolometric luminosity slightly greater than the Sun, with an effective temperature similar to the Sun, suggesting a subgiant classification. In the catalog of stellar properties derived from Gaia DR3 XP spectra (SHBoost; A. Khalatyan et al. 2024), its mass is estimated to be $M_{\mathrm{star}} = 0.98(12)\,M_{\odot}$, and a surface gravity[9] to be $\log_{10}(g) = 4.18(20)$, confirming that it is a G1V star, a subgiant with a temperature of 5854 K and luminosity of 2.1 $L\odot$. Table 2 lists the properties of this tertiary star.

We calculated the Gaia tertiary star coordinates in Table 2 to the pulsar's reference epoch (MJD 59997.5) using its measured proper motions, then compared them with the pulsar's timing-determined position, yielding an offset of 10 mas in R.A. and −3 mas in decl.. Based on the distance to the tertiary star inferred from the parallax, 2.1(4) kpc, and the offsets, the projected separation of the tertiary star and the pulsar in the sky plane can be estimated to be $S_{\perp} = 1.1(2) \times 10^4$ lt-s. Because their relative proper motions are $-0.82(9)$ mas yr^{-1} in the R.A. and $-0.1(2)$ mas yr^{-1} in the decl., their projected separation on the sky plane is decreasing, implying that the pulsar and the tertiary star are approaching each other. Note that the orbital motion of the tertiary star may lead to a systematic error in parallax measurement. However, for a not-so-wide phase range of the orbit, the proper motions and parallax measured by Gaia still reasonably describe the tertiary star's motion. A better description that accounts for orbital motion will be desired when the observational time span is comparable to the outer orbital period.

2.3. Initial Detection of the Gamma-ray Emission of PSR J0435+3233

We found that a gamma-ray source, 4FGL J0435.5+3232, in the fourth Fermi Large Area Telescope (LAT) point-source catalog (S. Abdollahi et al. 2022) is only 0.′8 away from PSR J0435+3233. To verify whether this gamma-ray source is the pulsar's counterpart, we folded the Fermi data using the ephemeris obtained from the FAST observations (Table 1). We extracted LAT photons with energies between 100 MeV and 300 GeV collected during the FAST timing span from the sky area within a 2° radius of the pulsar coordinates. Based on the radio pulsar ephemeris, we used the TEMPO2 Fermi plug-in to compute the phases of the photon arrival times (R. T. Edwards et al. 2006; G. B. Hobbs et al. 2006; P. S. Ray et al. 2011). Following the simple weight method of P. Bruel (2019) to calculate the photon weights, we folded the Fermi photon data in the FAST observation time span (MJD range 59101 to 60877) using the timing parameters in Table 1, and found that PSR J0435+3233 exhibits gamma-ray pulsations, with an H-test value of 69, confirming the pulsar's gamma-ray emission (see Figure 4(A)). While we were preparing the manuscript, we noticed that M. Zhang et al. (2026) obtained a similar result (with an H value of 63.9).

We show below that better-determined triple-system parameters improve the pulsar timing solution and extend the Fermi data span, yielding a much improved gamma-ray profile for this millisecond pulsar.

3. Constraints on the Properties of the Triple System

Since we have identified the tertiary star, the total mass of the triple system is $M_{\mathrm{t}} \equiv M_{\mathrm{PSR}} + M_{\mathrm{WD}} + M_{\mathrm{star}}$. Using FAST, optical/infrared, and Gamma-ray data, we aim to determine the parameters of the inner and outer orbits.

3.1. From Observed Pulsar Period Variations by FAST

The orbital parameters of the outer orbit can be constrained using the observed pulsar period variations caused by the orbital motion, which can be reconstructed from the pulsar timing results in Table 1 via

$$1/P(t) \equiv \nu(t) = \nu + (\dot{\nu} - \dot{\nu}_0)(t - t_0) + \frac{1}{2}\ddot{\nu}(t - t_0)^2 + ..., \quad (4)$$

[9] Note that the value of $\log_{10}(g) = 4.68$ in the original Gaia catalog DR3 (Gaia Collaboration et al. 2023) probably includes the contamination from a nearby luminous source about 7″ away.

Table 2
Optical/Infrared Parameters for the Tertiary

Parameter	Value	References
	Geometric parameters	
R.A., α (J2000)	$04^{h}35^{m}33^{s}.761275(4)$	(Gaia Collaboration et al. 2023)
decl., δ (J2000)	$+32^{\circ}33'07\farcs95514(4)$	(Gaia Collaboration et al. 2023)
Reference epoch	J2016.0	(Gaia Collaboration et al. 2023)
Proper motion in R.A. (mas yr^{-1})	0.694(84)	(Gaia Collaboration et al. 2023)
Proper motion in decl. (mas yr^{-1})	−3.530(63)	(Gaia Collaboration et al. 2023)
Parallax (mas)	0.466(78)	(Gaia Collaboration et al. 2023)
	Apparent magnitudes	
PS1 g (mag)	17.4601(42)	(K. C. Chambers et al. 2016)
Gaia DR3 BP (mag)	17.2978(63)	(Gaia Collaboration et al. 2023)
PS1 r (mag)	16.6684(24)	(K. C. Chambers et al. 2016)
Gaia DR3 G (mag)	16.6539(28)	(Gaia Collaboration et al. 2023)
PS1 i (mag)	16.2699(20)	(K. C. Chambers et al. 2016)
Gaia DR3 RP (mag)	15.8756(51)	(Gaia Collaboration et al. 2023)
TESS	15.9447(98)	(G. R. Ricker et al. 2015)
PS1 z (mag)	16.0625(33)	(K. C. Chambers et al. 2016)
PS1 y (mag)	15.9178(56)	(K. C. Chambers et al. 2016)
2MASS J (mag)	14.847(39)	(M. F. Skrutskie et al. 2006)
2MASS H (mag)	14.515(46)	(M. F. Skrutskie et al. 2006)
2MASS K_s (mag)	14.302(65)	(M. F. Skrutskie et al. 2006)
WISE W1 (mag)	14.256(59)	(M. F. Skrutskie et al. 2006)
WISE W2 (mag)	14.277(70)	(M. F. Skrutskie et al. 2006)
	SHBoost catalog parameters	
Surface gravity, $\log_{10}(g)$	4.18(20)	(A. Khalatyan et al. 2024)
Stellar mass, $M_{\rm star}$ ($M_\odot$)	0.98(12)	(A. Khalatyan et al. 2024)

Note. The geometry information, apparent magnitudes in different bands, and derived parameters for Gaia DR3 1718333951761382 40, which is exactly at the timing position of PSR J0435+3233. Numbers in parentheses represent 1σ errors in the final decimal.

where t_0 denotes the reference epoch, $\dot{\nu}_0$ accounts for the intrinsic spin-down, and t is the coordinate time of emission, which can be approximated by the infinite-frequency barycentre arrival time $t_{\rm b}$. We list the first five spin-frequency derivatives in Table 1, obtained by fitting the FAST observational data. The intrinsic spin-down $\dot{\nu}_0$ is largely coupled into the pulsar motions caused by orbital motion and cannot be directly determined.

The pulsar spin period varies with the outer orbital phase and can be expressed in terms of the orbital parameters by

$$\begin{aligned} P &= P_0\left(1+\frac{d\Delta_{\rm R2}}{dt}\right) \\ &= P_0 + P_0\frac{2\pi x_2 f_{\rm orb2}}{\sqrt{1-e_2^2}}[(\cos\theta_2+e_2)\cos\omega_2 \\ &\quad -\sin\theta_2\sin\omega_2], \end{aligned} \tag{5}$$

where P_0 is the intrinsic spin period of the pulsar, $\Delta_{\rm R2}$ is the Römer delay, θ_2 is the true anomaly, e_2 is the eccentricity, and ω_2 is the longitude of the periastron of the outer orbit. Here, θ_2 is related to the outer orbital frequency $f_{\rm orb2}\equiv 1/P_{\rm orb2}$ and the epoch of periastron passage of the outer orbit T_{02} via

$$\begin{aligned} E_2 - e_2\sin E_2 &= 2\pi f_{\rm orb2}(t-T_{02}), \\ \cos\theta_2 &= \frac{\cos E_2 - e_2}{1-e_2\cos E_2}, \\ \sin\theta_2 &= \frac{\sqrt{1-e_2^2}\sin E_2}{1-e_2\cos E_2}. \end{aligned} \tag{6}$$

Here, E_2 is the eccentric anomaly of the outer orbit. Since the period P depends linearly on $(\cos\theta_2+e_2)\cos\omega_2 - \sin\theta_2\sin\omega_2$, one can use linear regression to fit the model and quantify fit quality by the residual δP.

Because of its coupling with the outer orbit, this pulsar's intrinsic spin-frequency derivative, $\dot{\nu}_0$, cannot be measured directly as usual for a solitary pulsar or derived from measurements for binary pulsars. Assuming a characteristic age $\tau_c = -\nu/(2\dot{\nu}) = 10^{10}$ yr, a typical value for millisecond pulsars with a period of 3.2 ms, we preliminarily took $\dot{\nu}_0 = -4.95\times10^{-16}$ Hz s^{-1} —a better value will be determined later in the model fit. Ignoring the evolution of $\dot{\nu}_0$ and taking the tertiary mass of 1.0 $M_{\rm odot}$, we linearly set 16 observed spin periods over the MJD range covered by the FAST observations, and performed a four-dimensional grid search over $f_{\rm orb2}\in(1/2{,}000{,}000,\ 1/8000)d^{-1}$, $T_{02}\in(-P_{\rm orb2}/2,\ P_{\rm orb2}/2)$, $\omega_2\in(0^\circ,\ 180^\circ)$, and $e_2\in(0.0,\ 0.96)$ to minimize δP, with 1000–5000 grids for these parameters. Figure 5(A) shows the fitting results. From the FAST data alone, the eccentricity e_2 and the orbital frequency $f_{\rm orb2}$ are coupled and cannot be well determined from the best fit.

3.2. From the Gaia Geometry and Outer Companion Mass

For the semimajor axis of the relative outer orbit of the tertiary and the mass center of the pulsar and the WD, $a_{\rm out}$, which can be linked to the total mass $M_{\rm t}$ of the system via

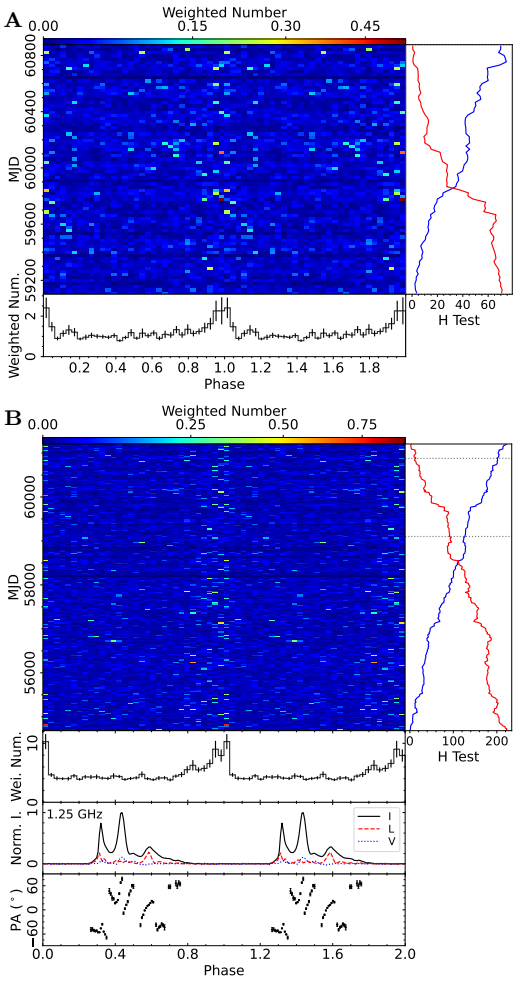


Figure 4. Phase histograms of gamma-ray photons for PSR J0435+3233 aligned with radio polarization profiles. Panel (A) is the result with the H-test value of $H \simeq 69$ for the Fermi data in the FAST observation duration (MJD: 59101—60877) and folded using the timing solution A with $i_x \sim 85^\circ$ (see Table 3). Note that folding Fermi data from MJD 59101 to 60783 yields $H \simeq 73$. Panel (B) shows the result from all available Fermi data (MJD: 54684—61205 ≃18 yr) using the final improved timing solution A, with the H-test factor reaching 221. The folding results of the timing solution B with $i_x \sim 54^\circ$ give similar H-test values. The error bars of the Fermi profile show the 1σ uncertainties, which are the square roots of the sum of squared weights. The lower two panels show timing-aligned radio polarization profiles at 1.25 GHz, showing a half-period offset from the Fermi profile. The total intensity I (solid line), linearly polarized intensity L (dashed line), and circularly polarized emission V (dotted line), with positive values for the left-hand sense, were obtained from 20 minute FAST observations on 2022 August 6, which has the highest signal-to-noise ratio. The bottom subpanel plots the linear polarization position angles (PAs), with uncertainties of $\pm 1\sigma$.

Kepler's third law,

$$\frac{a_{\rm out}^3}{P_{\rm orb2}^2} = \frac{GM_{\rm t}}{4\pi^2}. \quad (7)$$

The corresponding orbital inclination of the outer orbit i_2 can be deduced from

$$\sin i_2 = \frac{x_2}{a_{\rm out}} \frac{M_{\rm t}}{M_{\rm star}}. \quad (8)$$

Using the best-fit orbital parameters for different values of $P_{\rm orb2}$ and e_2, and adopting $M_{\rm star} = 1\,M_\odot$ and $S_\perp = 1.1 \times 10^4$ lt-s, we obtained the total mass of the triple system, $M_{\rm t}$, which has been constrained above in the range between 2.4 and 3.6 $M_\odot$. The distance between the barycentre of the inner binary and the outer companion can be expressed by

$$S_2^2 = S_\perp^2 + S_{\rm r}^2 = S_\perp^2 + \left(\frac{x_2(1-e_2^2)\sin(\theta_2+\omega)}{1+e_2\cos\theta_2} \frac{M_{\rm t}}{M_{\rm star}} \right)^2, \quad (9)$$

which is related to the semimajor axis of the relative orbit $a_{\rm out}$ of the outer binary through

$$S_2 = \frac{a_{\rm out}(1-e_2^2)}{1+e_2\cos\theta_2}. \quad (10)$$

From the four-dimensional grid search above for a physically viable set of orbital parameters, we found a solution with $M_{\rm t}$ in the range 2.4–3.6 $M_\odot$ and $\sin i_2 \leqslant 1$. As shown in Figure 5(B), we confirm that Gaia DR3 1718333951761382 40 is the outer companion of PSR J0435+3233, and that the tertiary orbital period is between 50 and 150 yr.

3.3. Integrating the Gravitational Three-body Effects on the Inner Orbit into TEMPO2

The inner companion is most likely a WD; in this case, the observed $\dot{f}_{\rm orb1}$ and $\dot{x}_1$ in Table 1 can constrain the orbital geometry. The observed $\dot{f}_{\rm orb1}$ is composed of

$$\dot{f}_{\rm orb1} = \dot{f}_{\rm orb1}^{\rm D} + \dot{f}_{\rm orb1}^{\rm tD} + \dot{f}_{\rm orb1}^{\rm t} + \dot{f}_{\rm orb1}^{\rm GW}, \quad (11)$$

where $\dot{f}_{\rm orb1}^{\rm D}$ originates from the classical Doppler effect, $\dot{f}_{\rm orb1}^{\rm tD}$ from *the transverse Doppler effect*, $\dot{f}_{\rm orb1}^{\rm t}$ from the perturbation by the outer companion, and $\dot{f}_{\rm orb1}^{\rm GW}$ from gravitational wave emission. The detailed expressions for the three-body terms $\dot{f}_{\rm orb1}^{\rm D}$, $\dot{f}_{\rm orb1}^{\rm tD}$ and $\dot{f}_{\rm orb1}^{\rm t}$ are given below, while $\dot{f}_{\rm orb1}^{\rm GW}$ is negligibly small. Similarly, the observed $\dot{x}_1$ can be written as

$$\dot{x}_1 = \dot{x}_1^{\rm D} + \dot{x}_1^{\rm tD} + \dot{x}_1^{\rm t}, \quad (12)$$

where the three contributions are, respectively, the classical Doppler term, the transverse Doppler term, and the perturbation from the outer companion.

If one takes the timing parameters of PSR J0435+3233 in Table 1 obtained from the FAST data, one can find small additional changes in the orbital period and projected semimajor axis of the inner orbit, exceeding the classic Doppler effect $\dot{f}_{\rm orb1}^{\rm D}$ and $\dot{x}_1^{\rm D}$ (T. Damour & J. H. Taylor 1992) by amounts of

$$\begin{aligned} \dot{f}_{\rm orb1} - \dot{f}_{\rm orb1}^{\rm D} &= \dot{f}_{\rm orb1} - \frac{\dot{\nu} - \dot{\nu}_0}{\nu} f_{\rm orb1} \\ &< -1.88(5) \times 10^{-22}\ {\rm s}^{-2}, \\ \dot{x}_1 - \dot{x}_1^{\rm D} &= \dot{x}_1 + \frac{\dot{\nu} - \dot{\nu}_0}{\nu} x_1 \\ &\approx 4.9 \times 10^{-13}\ {\rm lt\text{-}s\ s^{-1}}, \end{aligned} \quad (13)$$

where $\dot{\nu}_0$ is the unknown intrinsic spin-frequency derivative, and one can take the assumed value above. The small discrepancies likely originate from gravitational three-body effects in the triple system, which we consider in detail below.

For a triple pulsar, the *transverse Doppler effect* is the most significant relativistic contribution to the timing. The delay

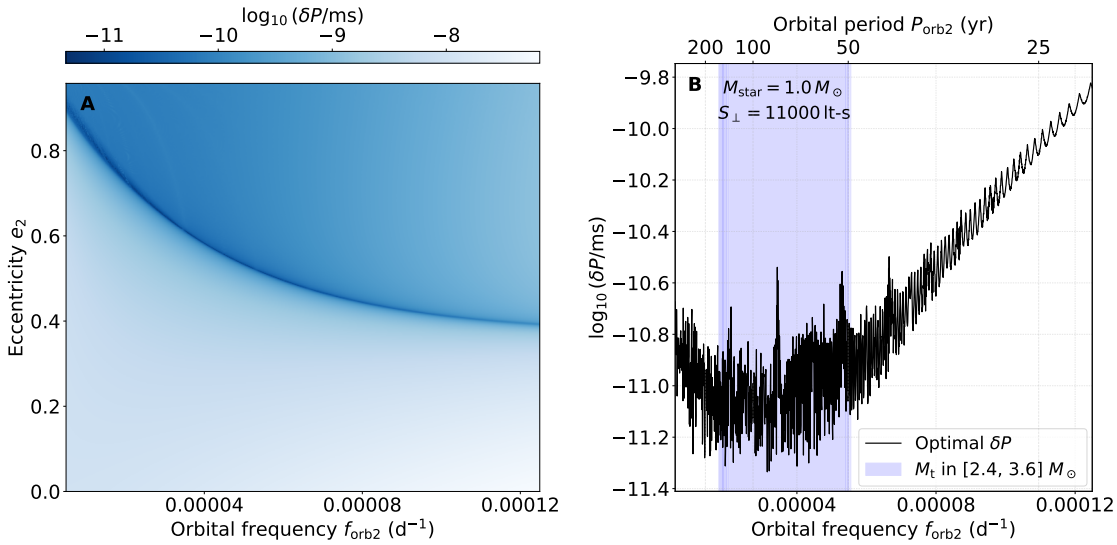


Figure 5. Preliminary constraints on the outer orbital parameters. Panel (A): residual distribution of the FAST-measured pulsar periods (δP in milliseconds) versus eccentricity e_2 and orbital frequency $f_{\rm orb2}$ ($\rm yr^{-1}$), plotted on a logarithmic scale. The best fits follow the darker curve, which shows the coupling between e_2 and $f_{\rm orb2}$. Panel (B): best-fit δP as a function of $f_{\rm orb2}$ for a given set of $M_{\rm star} = 1\ M_\odot$ and $S_\perp = 11{,}000$ lt-s constrained from the optical and infrared counterpart. The total mass $M_{\rm t}$ for the optimal orbital parameters should be in the range 2.4–3.6 $M_\odot$, with $f_{\rm orb2}$ highlighted by the shaded region, corresponding to the orbital period of the outer orbit $P_{\rm orb2}$ between 50 and 150 yr and the eccentricity e_2 between 0.50 and 0.75.

induced by this effect, $\Delta_{\rm tD}$, is given by the integral expression

$$\frac{d\Delta_{\rm tD}}{dt} = \frac{|\boldsymbol{v}_1 + \boldsymbol{v}_2|^2}{2} + \text{constant}, \tag{14}$$

where $\overrightarrow{v_1}$ is the pulsar's orbital velocity in the inner binary and $\boldsymbol{v}_2$ is the velocity of the inner binary's center of mass in the outer orbit. The contributions from v_1^2 and v_2^2 are parts of the Einstein delay (T. Damour & J. H. Taylor 1992). In a triple system, the cross term $\boldsymbol{v}_1 \cdot \boldsymbol{v}_2$ makes a unique contribution to the timing, as previously demonstrated in the case of the triple pulsar PSR J0337+1715 (S. M. Ransom et al. 2014). Since $\boldsymbol{v}_2$ varies much more slowly than $\boldsymbol{v}_1$ and the inner orbit is nearly circular, Equation (14) can be written as

$$\Delta_{\rm tD} = \int \boldsymbol{v}_1 dt \cdot \boldsymbol{v}_2 \approx a_1(v_{2,x}\cos\Phi_1 + v_{2,y}\sin\Phi_1), \tag{15}$$

where $v_{2,x}$ is the component of $\boldsymbol{v}_2$ along the ascending node of the pulsar's inner orbit, $v_{2,y}$ is the component perpendicular to it within the orbital plane, $a_1 \equiv x_1/\sin i_1$ is the pulsar's semimajor axis around the inner binary barycentre, and $\Phi_1 = 2\pi f_{\rm orb1}(t - T_{\rm asc1})$ is the mean anomaly. Combining $\Delta_{\rm tD}$ with the Römer delay $\Delta_{\rm R1}$, one get

$$\Delta_{\rm R1} + \Delta_{\rm tD} \approx (x_1 + a_1 v_{2,y})\sin\Phi_1 + a_1 v_{2,x}\cos\Phi_1. \tag{16}$$

One then can find an effective projected semimajor axis $x_1^{\rm eff}$ and an effective mean anomaly $\Phi_1^{\rm eff}$ for the inner orbit:

$$\begin{aligned} x_1^{\rm eff} &\approx x_1 + a_1 v_{2,y}, \\ \Phi_1^{\rm eff} &\approx \Phi_1 + \frac{v_{2,x}}{\sin i_1}. \end{aligned} \tag{17}$$

Consequently, the *transverse Doppler effect* induces a change in the inner orbital period of

$$\dot{f}_{\rm orb1}^{\rm tD} \approx \frac{1}{2\pi}\frac{d^2(v_{2,x}/\sin i_1)}{dt^2}. \tag{18}$$

It contributes to $\dot{x}_1$ by amount of

$$\dot{x}_1^{\rm tD} = \frac{d(a_1 v_{2,y})}{dt}. \tag{19}$$

In addition to the *transverse Doppler effect*, the tertiary perturbations cause variations of the inner orbit's parameters, which can be determined using the Lagrangian planetary equations (M. Valtonen & H. Karttunen 2006). We considered only the lowest-order term, the quadrupole term, in the perturbing function. For a nearly circular inner orbit, the time evolution of the inner orbital inclination angle i_1 driven by the tertiary perturbations is (F. A. Rasio 1994; K. J. Joshi & F. A. Rasio 1997)

$$\dot{i}_1^{\rm t} = \frac{3\pi}{P_{\rm orb1}}\frac{M_{\rm star}a_{\rm in}^3}{M_{\rm in}S_2^3}s_x s_z. \tag{20}$$

We have defined $s_x = S_{2,x}/S_2$, $s_y = S_{2,y}/S_2$, and $s_z = S_{2,z}/S_2$, where $S_{2,x}$, $S_{2,y}$, and $S_{2,z}$ denote the projections of S_2 in Equation (10) onto the respective directions. The time evolution of the inner orbit's projected semimajor axis caused by the tertiary perturbation is

$$\dot{x}_1^{\rm t} = x_1 \cot i_1\, \dot{i}_1. \tag{21}$$

In addition, the third-body perturbation can also modify $f_{\rm orb1}$. For a nearly circular orbit, $2\pi f_{\rm orb} = \dot{M} + \dot{\omega}$. According to the Lagrangian planetary equations, $\dot{f}_{\rm orb1}^{\rm t}$ is (M. Valtonen & H. Karttunen 2006)

$$\dot{f}_{\rm orb1}^{\rm t} = \frac{1}{P_{\rm orb1}}\frac{M_{\rm star}a_{\rm in}^3}{M_{\rm in}}\dot{Q}, \tag{22}$$

which is an important contribution to the inner orbital-frequency derivative from the tertiary. Here, $\dot{Q}$ describes the time variation of $Q = \left(3s_z^2 - \frac{3}{2}\cot i_1 s_y s_z - 1\right)/S_2^3$.

These effects should be able to produce the observed $\dot{f}_{\rm orb1}$, $\ddot{f}_{\rm orb1}$, $\dot{x}_1$, and $\ddot{x}_1$, providing further constraints on the orbital geometry of the triple system.

Following F. A. Rasio (1994) and K. J. Joshi & F. A. Rasio (1997), the tertiary perturbation also leads to the inner orbit's periastron advance and eccentricity evolution. According to the Lagrangian planetary equations, they can be written as

$$\begin{aligned}\dot{e}_1^{\rm t} &= -e_1\frac{15\pi}{P_{\rm orb1}}\frac{M_{\rm star}a_{\rm in}^3}{M_{\rm in}S_2^3}s_e\sqrt{1-s_z^2-s_e^2},\\ \dot{\omega}_1^{\rm t} &= \frac{3\pi}{P_{\rm orb1}}\frac{M_{\rm star}a_{\rm in}^3}{M_{\rm in}S_2^3}[5s_e^2+s_z^2\\ &\quad -\cot i_1 s_y s_z-2],\end{aligned}\tag{23}$$

where we have defined $s_e = S_{2,e}/S_2$, and $S_{2,e}$ is the component of $\overrightarrow{S_2}$ along the periastron passage of the inner orbit. GR also introduces a periastron advance that can be described by the first-order post-Newtonian (1PN) theory as (T. Damour & J. H. Taylor 1992)

$$\begin{aligned}\dot{\omega}_{\rm GR} &= 3\left(\frac{P_{\rm orb1}}{2\pi}\right)^{-5/3}(GM_{\rm in})^{2/3}(1-e_1^2)^{-1}\\ &\simeq 1.5\times10^{-4}\ {\rm rad/yr}.\end{aligned}\tag{24}$$

$\dot{\omega}_{\rm GR}$ are included in our timing analysis as slow changes of $\epsilon_1 \equiv e_1\sin\omega_1$ and $\epsilon_2 \equiv e_1\cos\omega_1$. However, because the inner orbit is very circular ($e_1 = 0.00016$), the small changes of $\dot{e}_1^{\rm t}$ and $\dot{\omega}_1^{\rm t}$ could be ignored in this current timing analysis.

In the above analysis, the perturbation potential is averaged over the inner orbital period $P_{\rm orb1}$. The tertiary perturbation also causes periodic changes of the inner orbital parameters within each $P_{\rm orb1}$. The magnitude of variations of Römer delay can be estimated by $\mathcal{K} = x_1 M_{\rm star}a_{\rm in}^3/(M_{\rm in}S_2^3) \sim 3\times10^{-8}$ s, and compared to current timing precision, such variations cannot be ignored. The orbital-parameter variations with the inner orbital phase Φ_1 can be derived from the Lagrangian planetary equations and expressed by:

$$\begin{aligned}\frac{\delta a_{\rm in}}{a_{\rm in}} &= \mathcal{K}\left[3s_x s_y\sin2\Phi_1+\frac{3}{2}(s_x^2-s_y^2)\cos2\Phi_1\right],\\ \delta i_1 &= \frac{3}{4}\mathcal{K}\,s_z(s_x\sin2\Phi_1 - s_y\cos2\Phi_1),\\ \delta\Phi_1 &= \mathcal{K}\left[\left(\frac{21}{4}s_x s_y+\frac{3}{4}s_z s_x\cot i_1\right)\cos2\Phi_1\right.\\ &\quad\left.+\left(-\frac{21}{8}(s_x^2-s_y^2)+\frac{3}{4}s_z s_y\cot i_1\right)\sin2\Phi_1\right],\\ \delta\epsilon_1 &= \mathcal{K}\left[\left(1-\frac{15}{4}s_x^2+\frac{3}{4}s_y^2\right)\sin\Phi_1+\frac{9}{2}s_x s_y\cos\Phi_1\right.\\ &\quad\left.+\frac{1}{4}(s_x^2-s_y^2)\sin3\Phi_1-\frac{1}{2}s_x s_y\cos3\Phi_1\right],\\ \delta\epsilon_2 &= \mathcal{K}\left[\left(1+\frac{3}{4}s_x^2-\frac{15}{4}s_y^2\right)\cos\Phi_1+\frac{9}{2}s_x s_y\sin\Phi_1\right.\\ &\quad\left.+\frac{1}{4}(s_x^2-s_y^2)\cos3\Phi_1+\frac{1}{2}s_x s_y\sin3\Phi_1\right].\end{aligned}\tag{25}$$

Their contribution to the Römer delay of the inner orbit $\Delta_{\rm R1}$ can be approximated as:

$$\begin{aligned}\delta\Delta R_1 &= x_1\cos\Phi_1\,\delta\Phi_1+\delta x_1\sin\Phi_1\\ &\quad-\frac{1}{2}x_1\,\delta\epsilon_1(\cos2\Phi_1+3)+\frac{1}{2}x_1\,\delta\epsilon_2\sin2\Phi_1.\end{aligned}\tag{26}$$

Combining Equations (25) and 26, we obtain

$$\begin{aligned}\delta\Delta_{\rm R1} &= \mathcal{K}x_1\left[-1+\frac{43}{16}s_x^2+\frac{5}{16}s_y^2+\frac{3}{4}s_y s_z\cot i_1\right]\sin\Phi_1\\ &\quad+\mathcal{K}x_1\left[-\frac{19}{8}s_x s_y+\frac{3}{4}s_x s_z\cot i_1\right]\cos\Phi_1\\ &\quad+\mathcal{K}x_1\frac{3}{16}(s_x^2-s_y^2)\sin3\Phi_1\\ &\quad-\mathcal{K}x_1\frac{3}{8}s_x s_y\cos3\Phi_1.\end{aligned}\tag{27}$$

The tertiary perturbation leads to systematic changes up to the $3\Phi_1$ term, affecting the Shapiro-delay measurements for the first three harmonics up to h_3, but not the fourth harmonic h_4.

Based on the three-body gravitational effects discussed above, we developed a new timing model in TEMPO2 (G. B. Hobbs et al. 2006) that employs the Keplerian orbital parameters of both orbits, the two orbital inclinations, the mutual inclination, and the total system mass to predict TOAs. The pulsar mass $M_{\rm PSR}$, WD mass $M_{\rm WD}$, and the outer companion mass $M_{\rm star}$ are derived from these parameters using Equations (1) and (7). The new timing formula is now expressed as

$$\begin{aligned}t_{\rm b} &= t+\left(1+\frac{d\Delta_{\rm R2}}{dt}\right)\Delta_{\rm R1}(t)+\Delta_{\rm R2}(t)\\ &\quad+\Delta_{\rm S1}(t)+\Delta_{\rm T}(t)+\Delta_{\rm E2}(t),\end{aligned}\tag{28}$$

where $t_{\rm b}$ is the barycentric arrival time, $\Delta_{\rm R2}$ is the Römer delay of the outer orbit, respectively, and $\Delta_{\rm S1}$ is the Shapiro delay of the inner binary, $\Delta_{\rm E2}$ is the Einstein delay of the outer orbit. The Shapiro delay and Einstein delay are calculated following T. Damour & J. H. Taylor (1992), assuming that GR is correct. The orbital parameters of the inner binary evolve under the perturbation of the outer companion, as given by Equations (21), (22), and (27). The orbital parameters of the outer orbit are evolving slowly, which can be calculated by numerical integration using the Lagrangian planetary equation with the perturbing function averaged over the inner orbital period.

3.4. Searching for Viable Geometry Parameters of the Triple System

Once the Keplerian orbital parameters of the two orbits are known, for a given $M_{\rm star}$ and $S_\perp$, the inclination angle of the outer orbit, i_2, and the total mass of the inner binary, $M_{\rm in}$, can be derived using Equations (9), (10), (7), and (8). Given the newly fitted Shapiro-delay parameter h_4 of the pulsar caused by the WD (see Table 1), one can also determine the inclination angle of the inner orbit, i_1, using Equation (2). Then, for a given relative angle between the orbits' ascending nodes, $\Delta\Omega = \Omega_2 - \Omega_1$, one can determine the relative orbital

orientation. The secular evolution of the inner orbit's parameters can be determined using Equations (19), (22), and (21).

Using the parameters from the grid search shown in Figure 5 in the area for $\delta P < 2\delta P_{\rm min}$ and adopting $M_{\rm star}$ in the range 0.62–1.34 $M_\odot$ with steps of 0.005 $M_\odot$, $S_\perp$ between 7000 and 15,000 lt-s with steps of 100 lt-s (the mass estimate is less reliable than the distance estimate), h_4 between $\pm 2\sigma_{h_4}$ with steps of 0.5 σ_{h_4}, and a pulsar mass between 1.1 and 2.2 $M_\odot$ (J. Alsing et al. 2018; B. Müller et al. 2025), we searched the value ranges of viable geometry parameters and also the full range of the relative ascending-node longitude $\Delta\Omega \equiv \Omega_2 - \Omega_1$ from 0 to 2π with 1000 steps, and evaluated the combined contributions of the different terms to $\dot{f}_{\rm orb1}$ and $\dot{x}_1$. A geometry is viable only when the predicted $\dot{x}_1$, $\ddot{x}_1$, $\dot{f}_{\rm orb1}$, and $\ddot{f}_{\rm orb1}$ simultaneously match the FAST TOA measurements within their 2σ uncertainties. We found two possible geometries; the inner and outer orbits are almost perpendicular, or they have a moderate mutual inclination of about 55° (see Figure 6). In fact, both $\Delta\Omega$ and $360^\circ - \Delta\Omega$ are possible solutions, corresponding to (i_1, i_2) and ($180^\circ - i_1$, $180^\circ - i_2$), respectively. However, the relative proper motion in Tables 1 and 2 excludes the possibility of $i_2 > 90^\circ$, as pointed out by P. Freire et al. (2026). Note also that the geometries are different from the coplanar orbits of the PSR J0337+1715 triple system (S. M. Ransom et al. 2014). Among all viable orbital geometries, the minimum δP is 4.5×10^{-12} ms, corresponding to Keplerian orbital parameters of $P_{\rm orb2} = 73.5$ yr, $e_2 = 0.597$, $x_2 = 2499$ lt-s, $T_{02} \simeq$ MJD 64812.8, and $\omega_2 = 32^\circ$.

3.5. Refining the Timing Solution of the Triple System from TOAs from Fermi and FAST Data

The Fermi data span MJD 54684 to 61205, a much longer time baseline than the FAST data. We can use both FAST and Fermi data to refine the triple-system timing solution. Using the best-fit Keplerian orbital parameters, orbital inclinations, and total system mass above, with small adjustments to the orbital parameters through the modified TEMPO2 fits for the triple system, we obtained a new timing solution for PSR J0435+3233 from the FAST TOA data. With this timing solution, we folded all available Fermi data and found that the pulsar's gamma-ray emission aligns well over almost the entire Fermi data span.

Next, we extracted 16 TOAs of PSR J0435+3233 from the Fermi data following P. S. Ray et al. (2011), which can provide constraints on the long-term variations caused by the outer orbit. We combined these TOAs with FAST TOAs to form a new set of TOAs. The coordinates, proper motion, and dispersion measure parameters were adopted from the previous best TEMPO2 fit, and then all TOA values were converted to the solar barycenter, which are used in the following nested sampling analysis. We then refined the model parameters using TEMPO2 (G. B. Hobbs et al. 2006) with the nested sampling technique based on the `ReactiveNestedCalibrator` function in ULTRANEST (E. Higson et al. 2019; J. Buchner 2021), with 4000 "live points" and a "log-evidence error" threshold of 0.1. The prior probability distribution for the transverse distance between the tertiary star and pulsar is taken in the range of $S_\perp = 1.1(2) \times 10^4$ lt-s, the pulsar mass in the range of $M_{\rm PSR} = 1.1$–$2.2\,M_\odot$ (J. Alsing et al. 2018; B. Müller et al. 2025), and the spin-frequency derivative of $\dot{\nu} < 0$. We found two sets of timing solutions, named solution A and solution B, as presented in Table 3. Figure 7 shows the probability distributions of the fitted parameters from the nested sampling. Figure 1 shows the projected orbits of the pulsar and its companions along our line of sight based on solution A. We fold the gamma-ray data with the two suites of timing solutions, achieving similar H-test values of 221 (see Figure 4). The timing residuals after fitting the data with the model parameters at the maximum-probability point of solution A (see Figure 2) are shown in Figure 8. The relative proper motion predicted by the geometries is about -0.7 mas yr^{-1} in R.A. and -0.5 mas yr^{-1} in decl., which is consistent with the observational results at the 2σ level. Figure 9 shows the predicted pulsar period variations along the outer orbital phase.

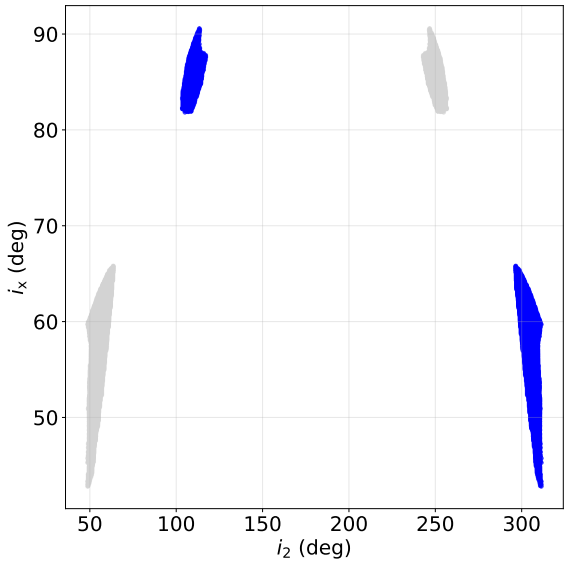


Figure 6. Possible ranges of the orbit inclination angles for the PSR J0435+3233 triple system. To explain the radio and optical/infrared results, the inner and outer orbits are either almost perpendicular or have a moderate mutual inclination of about $i_x = 54^\circ$. The gray regions were ruled out by the direction of relative proper motion between the pulsar and the outer companion.

4. Discussions

Based on the optical/infrared and gamma-ray archived data, we identified PSR J0435+3233 as a gamma-ray pulsar in a hierarchical triple system, with a He WD as a close inner binary companion and a Sun-like star as the distant tertiary. We determined the tertiary's outer elliptical orbit, with a period $P_{\rm orb2} = 73.5$ yr and an eccentricity $e_2 = 0.598$. This is a unique triple system for detailed multiband observations and for studying the evolutionary path and dynamic processes of a primordial triple star system.

4.1. Residual Perturbation From the Imperfect Timing Analysis for the Triple System

Because the tertiary orbit has limited phase coverage in the FAST and Fermi observations, it is hard to constrain the long- and short-term perturbations on the inner orbit from the tertiary. In the long term, the proper motion of the pulsar leads to variations of x_1, $P_{\rm orb1}$, x_2, and ω_2 through changes in line-of-sight direction (S. M. Kopeikin 1996), and the motion in the sky plane could not be approximated by a straight line, as pointed out by P. Freire et al. (2026). Fortunately, the

Table 3
Timing Parameters from Fitting Data with the Modified TEMPO2 Model and Key Derived Quantities for PSR J0435+3233

General Information		
FAST TOAs MJD range	59,101–60,877	
Number of FAST TOAs	192	
EFAC of FAST TOAs	0.97	
Fermi TOAs MJD range	54,887–61,001	
Number of Fermi TOAs	16	
EFAC of Fermi TOAs	1.53	
Solar System ephemeris	DE440	
Reference epoch (MJD)	59997.5	
Parameter	**Solution A**	**Solution B**
Basic pulsar parameters		
R.A., α (J2000)	$04^h35^m33^s.7608626(28)$	$04^h35^m33^s.7608612(28)$
decl. , δ (J2000)	$+32°33'07''.93347(17)$	$+32°33'07''.93354(17)$
Proper motion in R.A. (mas yr^{-1})	1.28(3)	1.27(3)
Proper motion in decl. (mas yr^{-1})	−3.29(15)	−3.33(15)
Spin frequency, ν (Hz)	312.7111521(5)	312.7111514(8)
Spin frequency derivative, $\dot{\nu}$ (Hz s^{-1})	$-8(8) \times 10^{-16}$	$2.6(16) \times 10^{-15}$
Inner Keplerian parameters for pulsar orbit		
Orbital period, $P_{\rm orb1}$ (day)	7.998147072(15)	7.998147028(22)
Projected semimajor axis, x_1 (lt-s)	7.9781313(4)	7.9780676(22)
Time of ascending-node passage, $T_{\rm asc1}$ (MJD)	59997.508015(8)	59997.508023(9)
First Laplace parameter, $\epsilon_1 = e_1 \sin\omega_1$	0.000139068(16)	0.000139073(21)
Second Laplace parameter, $\epsilon_2 = e_1 \cos\omega_1$	−0.000084130(12)	−0.000084130(13)
Inner orbital inclination, i_1 (deg)	107.7(6)	111.0(14)
Outer Keplerian parameters for inner binary barycenter		
Orbital period, $P_{\rm orb2}$ (day)	26,850(10)	26,872(19)
Projected semimajor axis, x_2 (lt-s)	2502.7(10)	2504.3(16)
Time of periastron passage, T_{02} (MJD)	64,802.8(4)	64,803.5(7)
Longitude of periastron passage, ω_2 (deg)	31.868(26)	31.81(5)
Orbital eccentricity, e_2	0.59822(6)	0.59825(6)
Outer orbital inclination, i_2 (deg)	146.3(11)	150.0(6)
Other fitting parameters		
System total mass, $M_{\rm t}$ ($M_\odot$)	2.35(10)	2.78(23)
Relative ascending-node longitude, $\Delta\Omega_{\rm asc}$ (deg)	108.1(12)	307.5(11)
Derived parameters		
Galactic longitude, l (deg)	168.15524	
Galactic latitude, b (deg)	−10.00888	
Pulsar spin period, P (s)	0.003197839256(5)	0.003197839282(8)
Pulsar mass, $M_{\rm PSR}$ ($M_\odot$)	1.16(5)	1.34(15)
Inner companion mass, $M_{\rm WD}$ ($M_\odot$)	0.273(8)	0.305(23)
Inner binary total mass, $M_{\rm in}$ ($M_\odot$)	1.44(6)	1.65(17)
Outer companion mass, $M_{\rm star}$ ($M_\odot$)	0.91(5)	1.13(7)
Mutual orbit inclination angle, $i_{\rm X}$ (deg)	84.9(8)	53.5(17)
Transverse distance between star and pulsar, $S_\perp$ (lt-s)	$1.190(19) \times 10^4$	$1.273(35)\times10^4$
Semimajor axis of the inner orbit, $a_{\rm in}$ (lt-s)	44.1(6)	46.1(16)
Eccentricity of the inner orbit, $e_{\rm in}$	0.000162535(15)	0.000162540(19)
Semimajor axis of the outer orbit, $a_{\rm out}$ (lt-s)	$1.164(16) \times 10^4$	$1.23(3) \times 10^4$
Semimajor axis of pulsar from inner binary barycenter, a_1 (lt-s)	8.376(27)	8.55(8)
Pulsar periastron longitude around inner binary barycenter, ω_1 (deg)	121.172(5)	121.171(5)
Pulsar ascending-node longitude around inner binary barycenter, Ω_1 (deg)	105	264
Semimajor axis of inner barycenter from triple barycenter, a_2 (lt-s)	$4.52(13) \times 10^3$	$5.01(9)\times10^3$
Ascending-node longitude of inner barycenter around triple barycenter, Ω_2 (deg)	213	212

Note. The reported values are the mean values of the posterior distributions, and numbers in parentheses are the standard deviations expressed in the magnitude of the last digits. We adopt the uncertainties of some fixed parameters (astrometric parameters and dispersion measure) in the nested sampling analysis from the TEMPO2 fit to FAST data. We took the prior ranges of $S_\perp = 1.1(2) \times 10^4$ lt-s, $\dot{\nu} < 0$, and $M_{\rm PSR} = 1.1$ to $2.2\,M_\odot$ for our analysis.

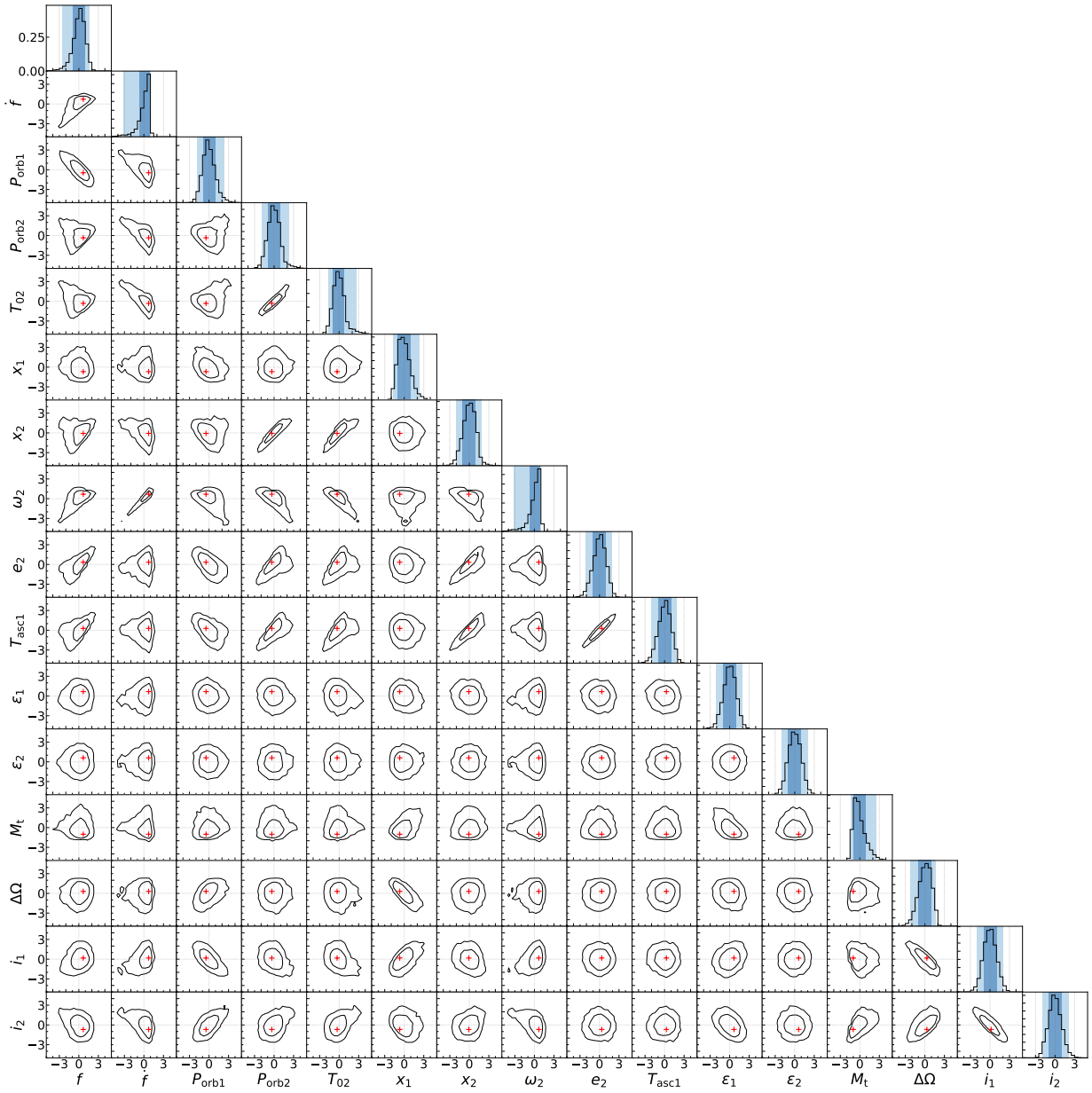


Figure 7. The probability distributions (corner plots) of the fitted parameters in the timing solution A in Table 3 (similar for solution B, not shown) using TEMPO2 (G. B. Hobbs et al. 2006). They are calculated using the nested sampling technique based on the `ReactiveNestedCalibrator` function in ULTRANEST (E. Higson et al. 2019; J. Buchner 2021). All parameters have been scaled by their mean and standard deviation, and all subpanels are plotted over the range $\pm5\sigma$ with two contour lines for the 68% and 95% possibilities. The red cross marks the maximum probability. The dark shadow in the histogram marks the $\pm1\sigma$ range, and the shallow shadow marks the $\pm2\sigma$ range.

deviation in TOAs caused by the changes in x_1, $P_{\rm orb1}$, and proper motion is about 10 ns in the FAST observational time span, smaller than the timing residuals. The TOA deviations caused by the changes in x_2 and ω_2 can be absorbed by small adjustments of other parameters. Therefore, ignoring these effects currently has little influence on the accuracy of the timing model. We ignored these effects in the above fittings.

From the current timing solutions based on limited FAST and Fermi data, errors in the predicted inner orbit induce timing residuals. In particular, in the folded Fermi gamma-ray data, photon pulse phases should change periodically at frequency harmonics of the inner orbital period. Because of limited photons, the integration time for each Fermi profile at a TOA is much longer than the inner-orbit period, so we cannot observe such residuals. However, changes in the long-term integrated profiles and the power at harmonics of the inner orbital period could be used to examine such imperfect timing solutions. As shown in Figure 10, we folded the Fermi gamma-ray profiles in the three MJD ranges and found that the profile in the range with embedded FAST observation duration is narrow, while the profiles in the earlier MJD durations are widened. We also analyzed the temporal power spectra of the pulsar spin-phase data from Fermi gamma-ray photons and found power at the exact frequency of the inner orbital period in the Fermi phase data from the early MJD range, implying that periodic perturbations in this triple system remain uncorrected.

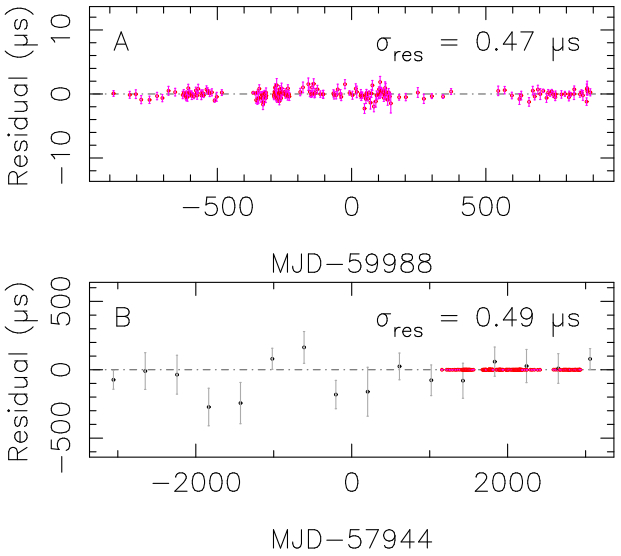


Figure 8. Timing residuals of PSR J0435+3233 based on the timing solution A. Panel (A) shows the timing residuals from FAST TOAs only, while panel (B) shows the timing residuals from Fermi TOAs (gray) and FAST TOAs. The timing residuals of solution B are almost the same.

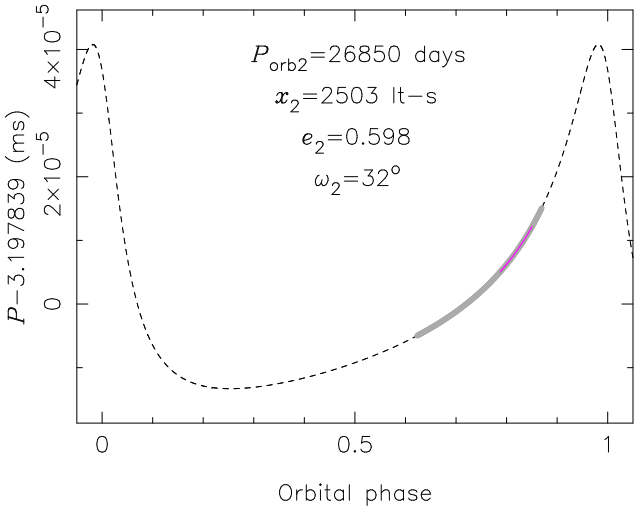


Figure 9. Predicted pulsar spin-period variations along the outer orbit based on the timing solution A. The orbital phase is defined as the mean anomaly measured from ω_2. The FAST observational time span occupies only a small fraction of the outer orbit, indicated by the magenta line. The Fermi data span is indicated by the thick gray line.

Despite imperfect timing from data in the limited tertiary orbital phase range, our analysis using the new timing model of the triple system still achieves high timing precision, yielding a Fermi integrated pulse profile with a high H-test value, which forms the basis for future studies of this system.

4.2. The Zeipel–Lidov–Kozai Effect

Concurrently, because the tertiary companion (M_{star}) orbits the center of mass of the inner subsystem on a wider and highly inclined orbit (∼85° or 54°), the inner binary might be subjected to von Zeipel–Lidov–Kozai (ZLK) eccentricity oscillations (S. Naoz 2016). The characteristic timescale of

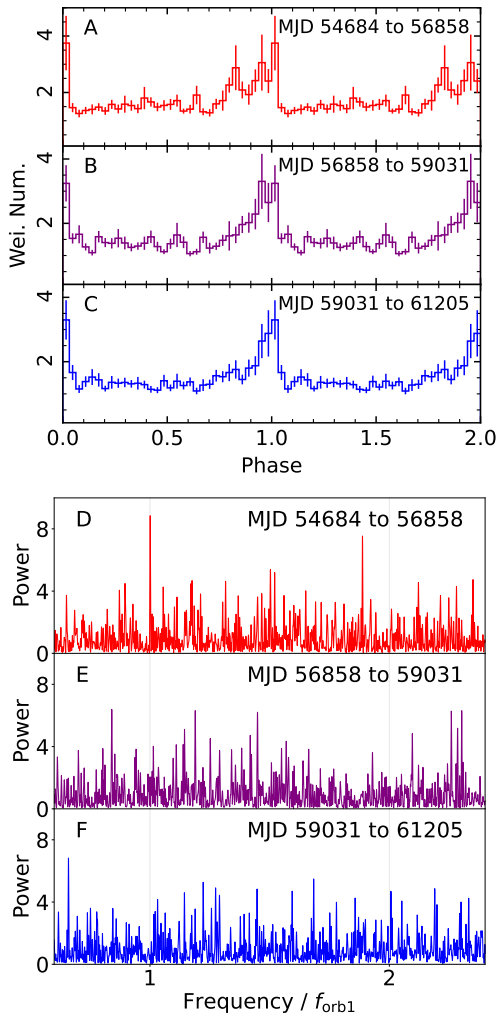


Figure 10. Three upper subpanels (A)–(C): folded Fermi gamma-ray profiles in the three MJD ranges with error bars for the 1σ uncertainty: (A) for MJD ∈ (54684, 56858), (B) for MJD ∈(56858, 59031), and (C) for MJD ∈ (59031, 61205). Compared with the profile in subpanel (C) with embedded FAST observation duration, the earlier MJD profiles are wider, implying uncorrected periodic perturbations from an imperfect ephemeris of this triple system. Three lower subpanels (D)–(F): temporal power spectra for the pulsar spin-phase data of Fermi gamma-ray photons in the three MJD ranges. Some uncorrected perturbations of the inner orbit from the tertiary in the timing model could induce some power at the exact frequency for the inner orbital period, as we do see in subpanel (D) for the early MJD range.

this secular process is

$$t_{\rm ZLK} = \frac{1}{n_{\rm in}}\frac{M_{\rm in}}{M_{\rm star}}\left(\frac{a_{\rm out}\sqrt{1-e_2^2}}{a_{\rm in}}\right)^3 \simeq 5\times10^4\ {\rm yr}\left(\frac{M_{\rm in}}{1.44M_\odot}\right)^{1/2}\left(\frac{M_{\rm star}}{0.91M_\odot}\right)^{-1}\left(\frac{a_{\rm in}}{44.1\ {\rm lt-s}}\right)^{3/2}\left(\frac{a_{\rm out}\sqrt{1-e_2^2}}{9327\ {\rm lt-s}}\right)^3.$$

Under the updated system parameters, the timescale for GR pericentre precession ($\sim 1/\dot{\omega}_{\rm GR} \sim 7\times10^3$ yr) is remarkably short compared to the ZLK timescale ($t_{\rm ZLK} \sim 5\times10^4$ yr). Consequently, the fast GR-induced precession overwhelmingly dominates the short-range dynamical force, completely

quenching the ZLK eccentricity excitation across all mutual inclinations I_0. Numerical integrations of the double-averaged secular equations of motion confirm that the inner orbit remains strictly near-circular ($e_1 \approx 0$) throughout its long-term evolution (B. Liu et al. 2015), experiencing no significant eccentricity growth regardless of the orbital alignment.

Given the highly inclined configuration observed today, the external tertiary was likely far from a passive spectator in the system's past; rather, it is highly probable that the tertiary played an active and important role in the early evolutionary history, particularly during the formation phase of the millisecond pulsar binary (D. Fabrycky & S. Tremaine 2007; S. Naoz et al. 2016; S. Toonen et al. 2016). Before the system settled into its current compact state, the primordial inner binary likely had a wider orbit, where secular gravitational perturbations from the misaligned tertiary could easily dominate short-range forces such as tidal dissipation and post-Newtonian effects. Under these conditions, large-amplitude ZLK oscillations would be efficiently excited, periodically driving the inner binary to extreme eccentricities and dramatically suppressing the periastron distance. Such gravitationally induced orbital shrinkage would naturally facilitate the onset of stable mass transfer or Roche–Lobe overflow, thereby assisting the recycling process that ultimately formed the millisecond pulsar–WD binary within this hierarchical framework.

4.3. Evolution of the PSR J0435+3233 Triple System

The PSR J0435+3233 triple system is located in the Galactic field, not in a dense cluster, so it is very probably evolved from the primordial triple system, i.e., of the three main-sequence (MS) stars born together, with masses of, for example, $20\,M_\odot$ for the pulsar progenitor, $2\,M_\odot$ for the WD progenitor, and $1\,M_\odot$ for the third star.

The formation pathway of PSR J0435+3233 is similar to the scenario proposed for PSR J0337+1715 (T. M. Tauris & E. P. J. van den Heuvel 2014). In this scenario, the inner binary initially consists of two stars with a relatively large mass ratio, leading to unstable mass transfer and a common-envelope phase. After the common envelope is ejected, a He star and an MS star remain in the inner binary. The He star subsequently undergoes a supernova explosion and forms an NS, which later accretes matter from the companion star and evolves into a millisecond pulsar with a He WD companion. Different from the PSR J0337+1715 formation scenario, the tertiary star has a sufficiently wide orbit and does not interact with the inner binary during the mass-transfer and recycling phases.

We investigated how supernova explosions in the inner binary, through sudden mass loss and natal kick, determine the survival probability of systems like PSR J0435+3233. Figure 11 shows the survival probability of the triple system as a function of the natal kick velocity (V_k) imparted to the newborn NS, where V_k is varied from 0 to $120\,\mathrm{km\,s^{-1}}$. Our simulations show that a triple system resembling PSR J0435+3233 can survive the supernova explosion provided that the V_k does not exceed $\sim 80\,\mathrm{km\,s^{-1}}$, corresponding to the recoil velocity immediately imparted to the inner binary (w_{12}) $\lesssim 40\,\mathrm{km\,s^{-1}}$. We found that even in the limiting case of a symmetric explosion ($V_k = 0$), the survival probability remains relatively low ($\sim$35%). We also explored the effects of varying the mass of the exploding star (and thus the ejecta mass) as well as the presupernova inner orbital period. A smaller amount of ejecta mass during the explosion could reduce w_{12} and therefore increase the survival probability. A wider presupernova inner orbital period also tends to increase the survival probability by reducing the recoil velocity. However, this advantage diminishes at higher natal kick velocities, where the wider inner binary is more easily disrupted during the supernova explosion.

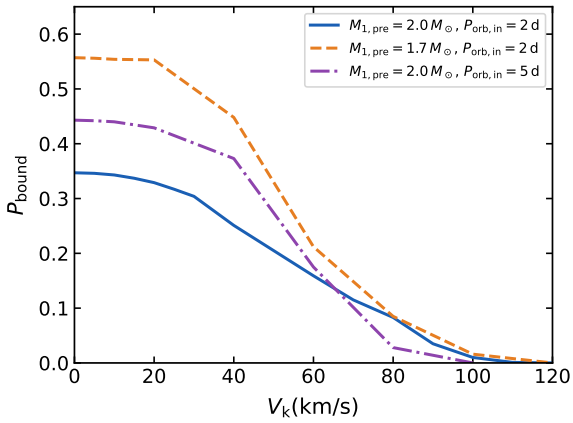


Figure 11. Survival probability of the triple system as a function of the natal kick velocity (V_k) imparted to the newborn NS. The basic model is plotted by a solid line for a presupernova inner binary with a He star with $M_{1,pre} = 2.0\,M_\odot$ at the presupernova stage, and an MS companion star with a mass of $2.0\,M_\odot$ in an initial orbital period ($P_{\mathrm{orb,in}}$) of 2 days, while the tertiary star has a mass of $1.3\,M_\odot$ and the outer orbit has a period of 30 yr. We set the newborn NS mass to $1.4\,M_\odot$. The dashed line is plotted for the alternative case with $M_{1,\mathrm{pre}} = 1.7\,M_\odot$, and the dashed–dotted line for the case with $P_{\mathrm{orb,in}} = 5$ days.

The tertiary star is located in a sufficiently wide orbit that no Roche–lobe overflow or other significant binary interaction with the inner binary is expected during its evolution. Consequently, it will evolve nearly as a single star and ultimately form a carbon-oxygen WD with a mass of $\sim 0.52\,M_\odot$. Because the tertiary loses mass during its late evolutionary stages, the outer orbit will expand gradually, resulting in a final orbital period of $\sim$70 yr. Combining the evolution of the inner binary and the tertiary star, the system will ultimately evolve into a system consisting of an NS, a He WD, and a carbon-oxygen WD tertiary companion.

Acknowledgments

The authors were supported by the National Key R&D Program of China No. 2025YFA1614002, the National Natural Science Foundation of China (NSFC), grant Nos. 12588202 and 12041303, and the Chinese Academy of Sciences via project JZHKYPT-2021-06.

This work used data from FAST (https://cstr.cn/31116.02.FAST). FAST is a Chinese national megascience facility, built and operated by the National Astronomical Observatories, Chinese Academy of Sciences. We all appreciate the excellent performance of FAST and the operation team. This publication makes use of data products from the Two Micron All Sky Survey (2MASS), which is a joint project of the University of Massachusetts and the Infrared Processing and Analysis Center/California Institute of Technology, funded by the National Aeronautics and Space Administration and the National Science Foundation. The Pan-STARRS1 Surveys (PS1) and the PS1 public science archive have been made possible through contributions by the Institute for Astronomy, the University of Hawaii, the Pan-STARRS Project Office, the

Max-Planck Society and its participating institutes, the Max Planck Institute for Astronomy, Heidelberg and the Max Planck Institute for Extraterrestrial Physics, Garching, The Johns Hopkins University, Durham University, the University of Edinburgh, the Queen's University Belfast, the Harvard-Smithsonian Center for Astrophysics, the Las Cumbres Observatory Global Telescope Network Incorporated, the National Central University of Taiwan, the Space Telescope Science Institute, the National Aeronautics and Space Administration under grant No. NNX08AR22G issued through the Planetary Science Division of the NASA Science Mission Directorate, the National Science Foundation grant No. AST-1238877, the University of Maryland, Eotvos Lorand University (ELTE), the Los Alamos National Laboratory, and the Gordon and Betty Moore Foundation. This work presents results from the European Space Agency (ESA) space mission Gaia. Gaia data are being processed by the Gaia Data Processing and Analysis Consortium (DPAC). Funding for the DPAC is provided by national institutions, in particular the institutions participating in the Gaia Multi-Lateral Agreement (MLA). The Gaia mission website is https://www.cosmos.esa.int/gaia. The Gaia archive website is https://archives.esac.esa.int/gaia. This work used Fermi-LAT data and software obtained from the Fermi Science Support Center (FSSC).

Facilities: FAST:500m, Fermi, Gaia, FLWO:2MASS, Pan-STARRS.

Software: Tempo2 (G. B. Hobbs et al. 2006), Ultranest (J. Buchner 2021), PSRCHIVE (A. W. Hotan et al. 2004), DSPSR (W. van Straten & M. Bailes 2011). Newly improved functions for the timing model are available on https://github.com/Zony-naoc/Timing-model-for-PSR-J0435-3233.

Author Contributions

J.L.H. identified problems, directed this project, organized the teamwork, checked the results, and finalized the Letter. Z.L.Y. solved all problems: reprocessed the FAST data, identified the optical tertiary, figured out its properties, found all related formulas caused by the outer orbit, implemented them into TEMPO2, obtained the timing solution from the radio, optical, and gamma-ray data, and drafted most parts of this Letter. Y.Y. processed the Fermi data and got the profiles based on the results from Z.L.Y., and drafted the relevant text. B.L. checked all possible terms of the relativistic effect for this specific triple system and drafted the relevant text. Y.L.G. and B.W. figured out the evolution routine of this triple system and drafted the relevant text. M.K.Y. worked out the properties of the Sun-like tertiary, and J.L., W.M.G., J.N.F., and B.W. joined the relevant discussions. L.H.L. worked out the optical plots used in this Letter. J.X. maintained the computer platform and data processing systems. All authors joined the discussions of results and contributed to finalizing the Letter.

ORCID iDs

Z. L. Yang https://orcid.org/0009-0009-6590-1540
J. L. Han https://orcid.org/0000-0002-9274-3092
Yi Yan https://orcid.org/0009-0008-1612-9948
Bin Liu https://orcid.org/0000-0002-0643-8295
Y. L. Guo https://orcid.org/0009-0008-2437-0184
M.K. Yang https://orcid.org/0009-0000-6595-2537
Bo Wang https://orcid.org/0000-0002-3231-1167
Wei-Min Gu https://orcid.org/0000-0003-3137-1851
J. Li https://orcid.org/0000-0002-2577-1990
L. H. Li https://orcid.org/0009-0007-5354-2611
J. Xu https://orcid.org/0000-0003-1778-5580
Jian-Ning Fu https://orcid.org/0000-0001-8241-1740

References

Abdollahi, S., Acero, F., Baldini, L., et al. 2022, ApJS, 260, 53
Alsing, J., Silva, H. O., & Berti, E. 2018, MNRAS, 478, 1377
Bruel, P. 2019, A&A, 622, A108
Buchner, J. 2021, JOSS, 6, 3001
Chambers, K. C., Magnier, E. A., Metcalfe, N., et al. 2016, arXiv:1612.05560
Damour, T., & Taylor, J. H. 1992, PhRvD, 45, 1840
Edwards, R. T., Hobbs, G. B., & Manchester, R. N. 2006, MNRAS, 372, 1549
Fabrycky, D., & Tremaine, S. 2007, ApJ, 669, 1298
Freire, P., Clark, C. J., Bassa, C. G., et al. 2026, arXiv:2607.27462
Freire, P. C. C., & Wex, N. 2010, MNRAS, 409, 199
Gaia Collaboration, Prusti, T., de Bruijne, J., H., J., et al. 2016, A&A, 595, A1
Gaia Collaboration, Vallenari, A., Brown, A. G. A., et al. 2023, A&A, 674, A1
Higson, E., Handley, W., Hobson, M., & Lasenby, A. 2019, MNRAS, 483, 2044
Hobbs, G. B., Edwards, R. T., & Manchester, R. N. 2006, MNRAS, 369, 655
Hotan, A. W., van Straten, W., & Manchester, R. N. 2004, PASA, 21, 302
Iorio, L. 2024, Univ, 10, 206
Jiang, P., Tang, N.-Y., Hou, L.-G., et al. 2020, RAA, 20, 064
Joshi, K. J., & Rasio, F. A. 1997, ApJ, 479, 948
Khalatyan, A., Anders, F., Chiappini, C., et al. 2024, A&A, 691, A98
Kopeikin, S. M. 1996, ApJL, 467, L93
Lange, C., Camilo, F., Wex, N., et al. 2001, MNRAS, 326, 274
Li, D., Wang, P., Qian, L., et al. 2018, IMMag, 19, 112
Liu, B., Muñoz, D. J., & Lai, D. 2015, MNRAS, 447, 747
Mardling, R. A., & Aarseth, S. J. 2001, MNRAS, 321, 398
Moe, M., & Di Stefano, R. 2017, ApJS, 230, 15
Müller, B., Heger, A., & Powell, J. 2025, PhRvL, 134, 071403
Nan, R. 2006, ScChG, 49, 129
Naoz, S. 2016, ARA&A, 54, 441
Naoz, S., Fragos, T., Geller, A., Stephan, A. P., & Rasio, F. A. 2016, ApJL, 822, L24
Portegies Zwart, S., van den Heuvel, E. P. J., van Leeuwen, J., & Nelemans, G. 2011, ApJ, 734, 55
Ransom, S. M., Stairs, I. H., Archibald, A. M., et al. 2014, Natur, 505, 520
Rasio, F. A. 1994, ApJL, 427, L107
Ray, P. S., Kerr, M., Parent, D., et al. 2011, ApJS, 194, 17
Ricker, G. R., Winn, J. N., Vanderspek, R., et al. 2015, JATIS, 1, 014003
Sabach, E., & Soker, N. 2015, MNRAS, 450, 1716
Shao, L. 2016, PhRvD, 93, 084023
Skrutskie, M. F., Cutri, R. M., Stiening, R., et al. 2006, AJ, 131, 1163
Tauris, T. M., & Savonije, G. J. 1999, A&A, 350, 928
Tauris, T. M., & van den Heuvel, E. P. J. 2014, ApJL, 781, L13
Thorsett, S. E., Arzoumanian, Z., Camilo, F., & Lyne, A. G. 1999, ApJ, 523, 763
Toonen, S., Hamers, A., & Portegies Zwart, S. 2016, ComAC, 3, 6
Valtonen, M., & Karttunen, H. 2006, The Three-Body Problem (Cambridge: Cambridge Univ. Press)
van Straten, W., & Bailes, M. 2011, PASA, 28, 1
Voisin, G., Cognard, I., Freire, P. C. C., et al. 2020, A&A, 638, A24
Wright, E. L., Eisenhardt, P. R. M., Mainzer, A. K., et al. 2010, AJ, 140, 1868
Wu, Q., Wang, N., Yuan, J., et al. 2026, NatAs, 10, 1020
Zhang, M., Pei, S., & Zhang, P. 2026, arXiv:2607.16119